Structural basis of inhibition of human $Na_V1.8$ by the tarantula venom peptide Protoxin-I

Bryan Neumann[1], Stephen McCarthy[1], Shane Gonen[1*]

[1] Department of Molecular Biology and Biochemistry, University of California Irvine, CA 92617, USA
* to whom correspondence should be addressed

Shane Gonen: gonens@uci.edu

Abstract

Voltage-gated sodium channels (Na_Vs) selectively permit diffusion of sodium ions across the cell membrane and, in excitable cells, are responsible for propagating action potentials. One of the nine human Na_V isoforms, $Na_V1.8$, is a promising target for analgesics, and selective inhibitors are of interest as therapeutics. One such inhibitor, the gating-modifier peptide Protoxin-I derived from tarantula venom, blocks channel opening by shifting the activation voltage threshold to more depolarised potentials, but the structural basis for this inhibition has not previously been determined. Using monolayer graphene grids, we report the cryogenic electron microscopy structures of full-length human apo-$Na_V1.8$ and the Protoxin-I-bound complex at 3.1 Å and 2.8 Å resolution, respectively. The apo structure shows an unexpected movement of the Domain I S4-S5 helix, and VSD_I was unresolvable. We find that Protoxin-I binds to and displaces the VSD_{II} S3-S4 linker, hindering translocation of the $S4_{II}$ helix during activation.

Keywords

$Na_V1.8$, cryoEM, Protoxin-I, graphene, voltage-gated sodium channel

Introduction

Voltage-gated sodium channels (Na_Vs) are integral membrane proteins responsible for the selective permeation of sodium ions into cells in response to membrane depolarization. The small differences in sequence that characterize the nine human Na_V subtypes ($hNa_V1.1$-1.9, Supplementary Figure 1) nonetheless give rise to distinct electrophysiological properties that, together with varying expression levels in different tissues, give each hNa_V isoform particular roles in sensation.

$Na_V1.8$, one of the three tetrodotoxin-resistant Na_Vs, is distinguished from other isoforms by the relatively depolarized voltage-dependency of activation and inactivation, slower inactivation kinetics, and a higher persistent current;[1–3] These attributes make $Na_V1.8$ principally responsible for inward currents during the rising phase of the action potential,[4,5] and contribute to hyperexcitability and repetitive firing in the dorsal root ganglion (DRG) neurons where it is primarily localised.[6,7] Uniquely, it maintains its gating properties at cold temperatures.[8]

Multiple studies have linked $Na_V1.8$ to nociception and chronic pain. Gain-of-function mutations in $Na_V1.8$ causing increased excitability of DRG neurons have been identified in patients with peripheral neuropathy,[9,10] while a loss-of-function $Na_V1.8$ mutation has been linked to reduced pain sensation.[11,12] $Na_V1.8$ has also been linked to inflammatory pain.[13] Studies of Grasshopper mice (*Onychomys torridus*) showed that their insensitivity to pain

induced by the venom of the Arizona bark scorpion (*Centruroides exilicauda*) derives from mutations in their $Na_V1.8$ channels;[14] injection of the venom reduced the *O. torridus* pain response to the formalin test, demonstrating that inhibition of $Na_V1.8$ is a viable analgesic strategy.[15]

Inhibitors of $Na_V1.8$ are therefore of interest as pain treatments, and peptides derived from animal venom are renowned modulators of Na_V activity. Unlike small-molecule inhibitors, which typically bind in the highly conserved pore domain, peptide inhibitors frequently bind to the less-conserved extracellular regions above the voltage-sensing domains (VSDs) which provide greater scope for isoform selectivity in drug development. $Na_V1.8$-selective peptides include scorpion venom peptide BmK I,[16] the μ-conotoxins MrVIA/MrVIB[17,18] and TsIIIA,[19] and the tarantula venom peptide Protoxin-I (ProTx-I).[20]

ProTx-I is isolated from the venom of the Peruvian green velvet tarantula (*Thrixopelma pruriens*) and is a gating-modifier peptide that shifts the voltage-dependence of activation to more depolarized potentials.[20] It shows slight selectivity for rat $Na_V1.8$ (IC_{50} = 27 nM)[21] over other human Na_V isoforms (typically IC_{50} = 60-130 nM),[22] as well as activity against T-type calcium channels[23] and the TRPA1 channel.[24] ProTx-I is disulfide-rich and shares the inhibitor cystine knot (ICK) framework that is common among gating-modifier tarantula venom peptides.[25] Mutagenesis studies using $hNa_V1.7/K_V2.1$ chimeras localized the binding site of ProTx-I to $Na_V1.7$ on the extracellular loops of VSD_{II} and VSD_{IV}[26] but the exact binding mechanism remained undetermined.

Structural characterisation of venom peptides in complex with Na_Vs is essential for understanding their pharmacological profiles and for realizing their potential as tool compounds and drugs. However, poor Na_V expression yields and low local resolution for bound peptides have made these structures difficult to obtain. Full-length Na_V-peptide complexes determined to date are limited to $Na_V1.2$ in complex with the pore-blocking μ-conotoxin KIIIA,[27] $Na_V1.5$ bound to the scorpion venom peptide LqhIII,[28] and the American cockroach channel Na_VPaS bound to the spider venom peptide Dc1a.[29] Attempts to characterise complexes of human $Na_V1.7$ with the spider venom peptides Protoxin-II and Huwentoxin-IV produced high-resolution reconstructions of the channel but could not sufficiently resolve the peptide for modeling.[30] Chimeric channels consisting of bacterial or invertebrate Na_V scaffolds onto which human Na_V domains have been grafted have also been developed to address this problem. A $Na_VAb/Na_V1.7$-VSD_{II} chimera was used to determine the binding mechanism of Protoxin-II and Huwentoxin-IV,[31] which has additionally been characterised in complex with a $NaChBac/Na_V1.7$-VSD_{II} chimera,[32] while a $Na_V1.7$-VSD_{IV} chimera based on the Na_VPaS scaffold aided in characterisation of the scorpion venom peptide AaH2 as well as small molecule inhibitors.[33]

Mutagenesis screening and chimeric constructs can be effective in identifying channel variants with higher expression yield, but mutations can affect channel gating properties and chimeric constructs lack functional domains.[34] Experimental structures with full-length human channels are therefore preferred for rational structure-based drug design in order to minimise off-target interactions; maximising yield and particle grid density through mammalian cell expression, biochemical and cryogenic electron microscopy (cryoEM) developments is therefore an attractive strategy.

As of yet, no Na_V-bound structure of ProTx-I has been determined. Here, we used mammalian HEK293 cells to express full-length human $Na_V1.8$ and determined the structure, with and without ProTx-I bound, by single-particle cryoEM. Optimisation of the expression and purification, and the use of monolayer graphene grids, allowed the maximum number of useable particles for data collection from as low as 1.5 L of cell culture. The final reconstructions were determined at an overall resolution of 3.1 Å for apo-$hNa_V1.8$ and 2.8 Å for the $hNa_V1.8$-ProTx-I complex. Separate classifications revealed large movements of the

S4-S5 linker leading to VSD_I, and consequently this voltage-sensing domain was unresolvable. The resolution of the map in the ProTx-I region was sufficient for tracing of the peptide backbone and determination of its mechanism of binding. We anticipate that the developed protocols will be beneficial in the solution of future peptide-Na_V complexes by cryoEM, and that these results will assist in the design of novel drugs targeting hNa_V1.8.

Results

Apo-hNa_V1.8

Human Na_V1.8 α-subunit was co-expressed in HEK293 cells together with the β4-subunit and purified as described in Methods. Na_V α-subunits are frequently co-expressed with β-subunits to stabilise the protein, increase expression levels, and maintain a more native environment. Evidence suggests that hNa_V1.8 is capable of interacting with all four β-subunits, including β4, which affects hNa_V1.8 activation and inactivation thresholds.[35] However, despite co-expression, only the α-subunit was observed after purification (Supplementary Figure 2) and in the final map; loss of co-expressed β-subunits has been observed for other Na_Vs[36–38]and may reflect weak binding affinity between the proteins (see Discussion). To maximise the final hNa_V1.8 yield, several parameters were screened (see Methods) and the overall time between solubilization and purification was minimized. Prior to cryoEM, particle purity and homogeneity were confirmed by negative stain (Supplementary Figure 2d).

Screening freezing conditions using conventional holey carbon grids showed a preference for particles to accumulate over the carbon film, and low particle density in the holes (Supplementary Figure 3a). Due to low yields, we attempted to increase the scale of the cell culture, but this introduced problems with solubilization and did not sufficiently increase the final usable protein concentration. The initial grid screening included a range of grid types, including one with a support film of monolayer graphene which showed improved particle distribution across the grid holes (Supplementary Figure 3a). We therefore pursued the use of support film grids, including monolayer graphene, as an alternative to mutagenesis or large increases in the scale of cell culture. Using ultrathin (2-3 nm) carbon grids under similar conditions failed to produce a cryoEM dataset that could reach high resolution (data not shown) which we hypothesize was due to contrast loss resulting from particle packing. Graphene oxide grids indicated acceptable Na_V particle density and contrast but were more susceptible to breakage from glow discharging (Supplementary Figure 3b). All maps in this manuscript resulted from the use of monolayer graphene grids (0.4 nm thickness) which showed good particle distribution and contrast (Supplementary Figure 3c); this allowed us to reconstruct the structures using just ~0.15 mg/mL of purified protein from as low as ~20 g wet cell pellet or 1.5 L of cell culture, significantly lower than typical Na_V preparations.[37,39–41]

This approach allowed us to reconstruct apo-hNa_V1.8 at an overall resolution of 3.1 Å (Figure 1; Supplementary Figures 4 and 5; Supplementary Table 1). Typical of other apo-Na_V structures, the apo model shows features characteristic of an inactivated channel, with gating charge residues on all visible VSDs showing ‘up’ conformations (Supplementary Figure 5) and the IFM fast inactivation motif on the VSD_{III}-VSD_{IV} linker buried in its binding site between $S6_{IV}$, $S5_{IV}$ and the VSD_{III} S4-S5 linker (Figure 1a,c). The quality of the map allowed modeling of glycosylation at several positions on the extracellular loops, as well as possible cholesterol, lipids, and detergent molecules bound to the transmembrane region; similar to other cryoEM structures of Na_V channels we observe density for a bound molecule in the intracellular pore region, which we putatively assign as cholesterol (Figure 1c,e).[27,34,36,39,40]

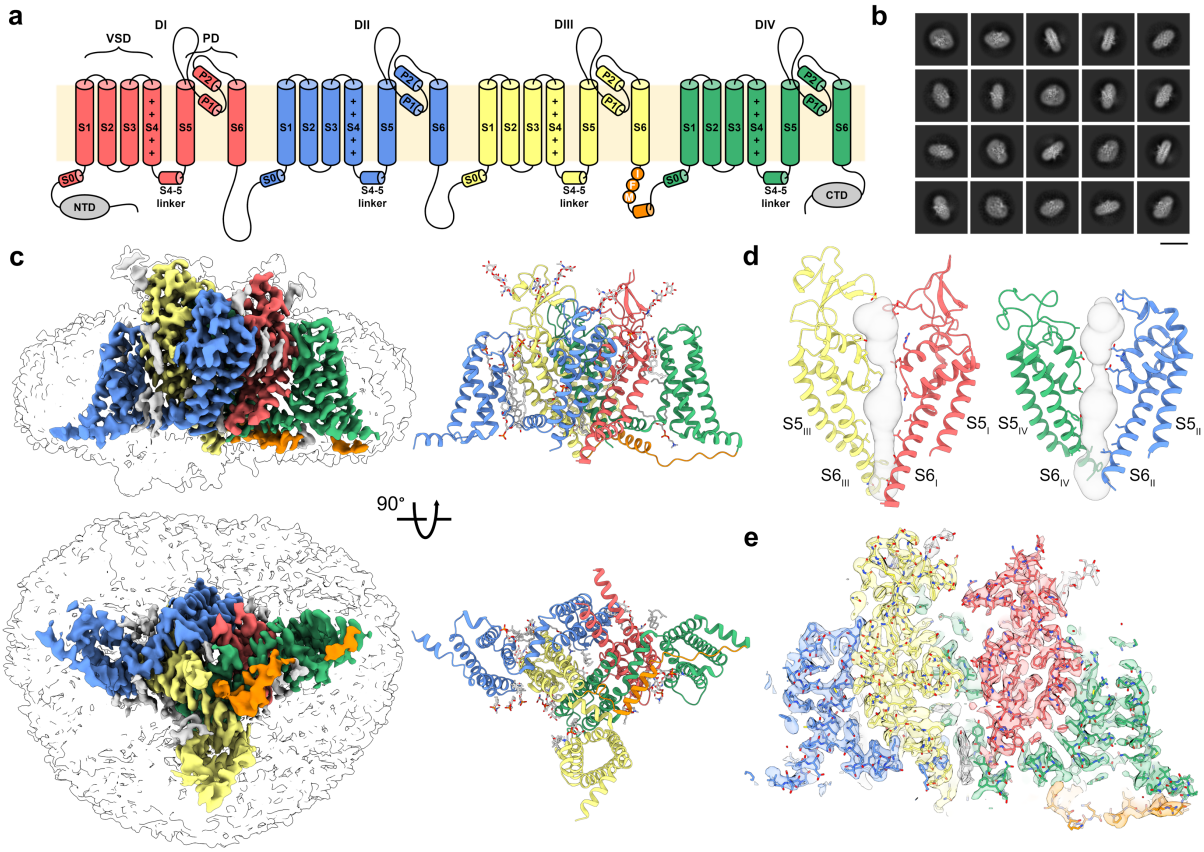

Figure 1: Overall architecture and reconstruction of apo-hNa$_V$1.8
a Topology of hNa$_V$s colored by domain: DI (red), DII (blue), DIII (yellow) and DIV (green). **b** Example 2D class averages for apo-hNa$_V$1.8; scale bar = 15 nm. **c** (left) Side and intracellular views of the final apo-hNa$_V$1.8 map (colored according to the scheme in **a**) with transparent lower map threshold to indicate micelle and emerging NTD, and (right) the resulting final refined model. Glycosylation and small molecule ligands, including cholesterol in the pore are shown in grey. **d** Two views of the apo-hNa$_V$1.8 pore domain showing the ion permeation path in grey. **e** Model-to-map fit for a central cross-section of apo-hNa$_V$1.8.

Density corresponding to VSD$_I$ is almost entirely absent in the 2D and 3D classifications, and in the final reconstruction (Figure 1b,c), even as portions of the N-terminal domain (NTD) can be observed at lower map thresholds; this result is consistent with a prior report.[36] Attempts to improve the resolution in this region through 3D classifications steps, masking, and local refinements did not improve interpretability of VSD$_I$ but did reveal separate classes (denoted Class I and Class II, Supplementary Figure 4) showing a distinct repositioning of the VSD$_I$ S4-S5 linker and a smaller movement of the lower portion of the VSD$_I$ S6 helix (Figure 2, Supplementary Movie 1); The final apo map and structure was calculated from all particles making up Class I and Class II. In Class I the VSD$_I$ S4-S5 linker is positioned closer to the pore domain even as S6$_I$ moves outwards (Figure 2c, cyan arrows), while in Class II the VSD$_I$ S4-S5 linker swings outwards (Figure 2c, purple arrows); the S6$_I$ helix moves contrarily and tucks closer into the pore. In all our reconstructions, the VSD$_I$ S4-S5 linker is positioned significantly outward (by up to 17 Å) compared to the prior apo-Na$_V$1.8 structure (PDB 7WFW).[36] These movements necessarily affect the positioning, and likely contribute to the unresolvability, of VSD$_I$; this is supported by 3D variability analysis, where, at low thresholds, density of the NTD is observed in slightly different positions (Supplementary Movie 2). Distinct positions for NTD and VSD$_I$ have also been observed in Na$_V$1.7-M11, an engineered variant of hNa$_V$1.7 containing 11 mutations that collectively induce a large depolarizing shift in the activation voltage,[42] underlining the connection between VSD$_I$ lability and activation thresholds.

Analysis of the ion permeation path shows the point of greatest restriction around the selectivity filter in the upper pore and is similar in all structures (Figure 2a). The pore diameter through the intracellular gate is ~3 Å, consistent with the conformation of the S6 helices observed in hNa$_V$1.7[34] and which allows space for the bound cholesterol molecule in our maps.

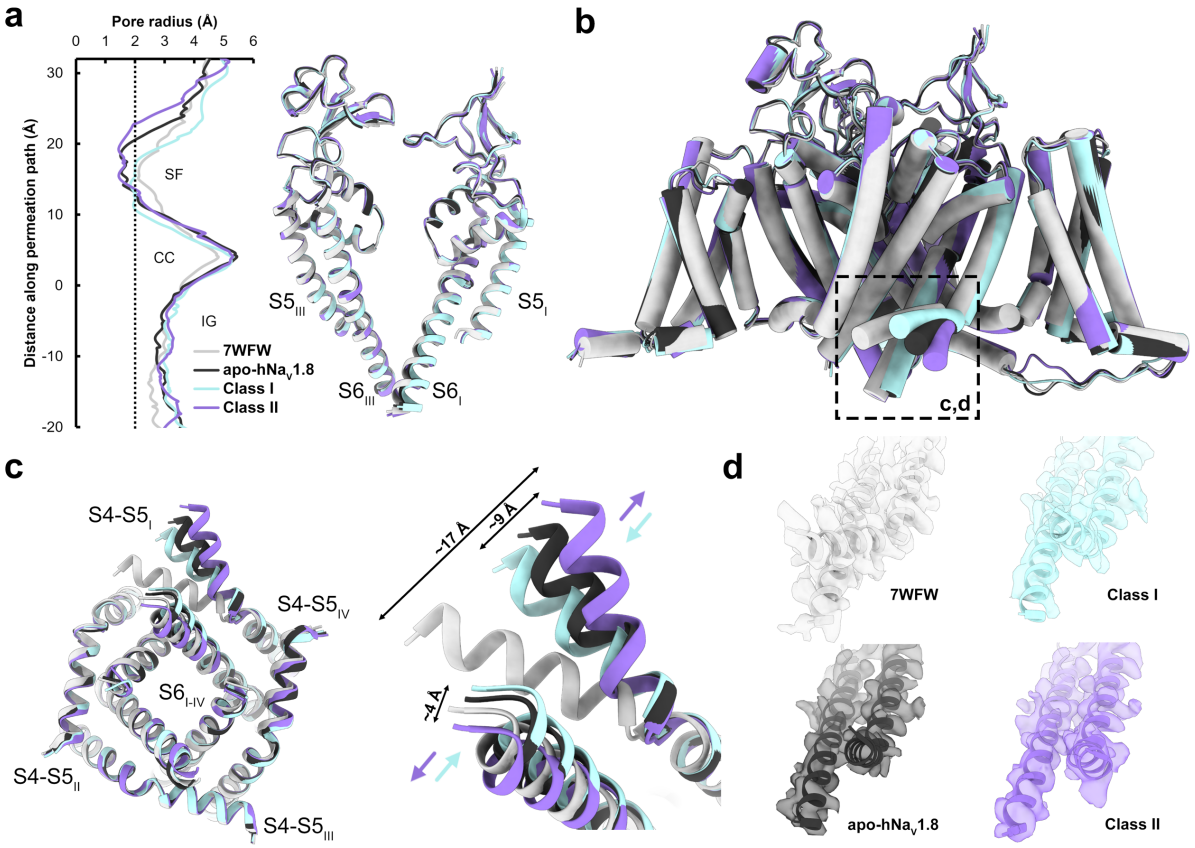

Figure 2: Structural comparisons of apo-hNa$_V$1.8, highlighting dynamics of VSD$_I$ S4-S5 linker and S6 helices

a (left) Pore radius for the overall apo-hNa$_V$1.8 model (black) together with Class I (cyan), Class II (purple), and 7WFW (light grey),[36] and (right) aligned pore domains showing minimal backbone movements. The selectivity filter (SF), central cavity (CC) and intracellular gate (IG) are indicated. **b** Comparison of the four apo-hNa$_V$1.8 models contrasting the close overall structural agreement with the extensive outward movement of the VSD$_I$ S4-S5 linker (dashed black box). **c** (left) Intracellular view of the pore domain showing movements of the VSD$_I$ S4-S5 linker and lower S6$_I$ helix, with (right) close-up views highlighting the angular displacements (indicated by color-coded arrows) of the VSD$_I$ S4-S5 linker and S6 helix. Displacements between Class I and Class II measure ~9 Å for the VSD$_I$ S4-S5 linker and ~4 Å for the S6 helix **d** Model-to-map fits of the VSD$_I$ S4-S5 linker for all apo-hNa$_V$1.8 structures.

ProTx-I-bound complex

The hNa$_V$1.8-ProTx-I complex was prepared by incubating ProTx-I solution with purified apo-hNa$_V$1.8 prior to freezing with monolayer graphene grids. We observed low particle contrast during initial screening using carbon support grids, in part due to excess ProTx-I; we therefore introduced ProTx-I prior to a final concentration step to remove unbound peptide. Processing of the data produced a map with an overall resolution of 2.8 Å from 267,708 particles (Figure 3; Supplementary Figures 6 and 7). Outside the ProTx-I binding region, the refined hNa$_V$1.8 structure in the complex is very similar to apo-hNa$_V$1.8, with some slight rigid-body shifts in the VSDs and small movements in the extracellular loops. The higher resolution of this map, likely enabled by the stabilising effect of ProTx-I, allowed an additional extracellular loop (ECL$_I$, D280-P295) to be traced in the hNa$_V$1.8-ProTx-I map that was not possible for apo-hNa$_V$1.8 (Supplementary Figure 7). The VSD$_I$ S4-S5 linker is again swung outward and consequently

225 VSD_I is not resolvable, despite additional processing, a larger dataset, and the higher overall
226 resolution of the reconstruction.
227

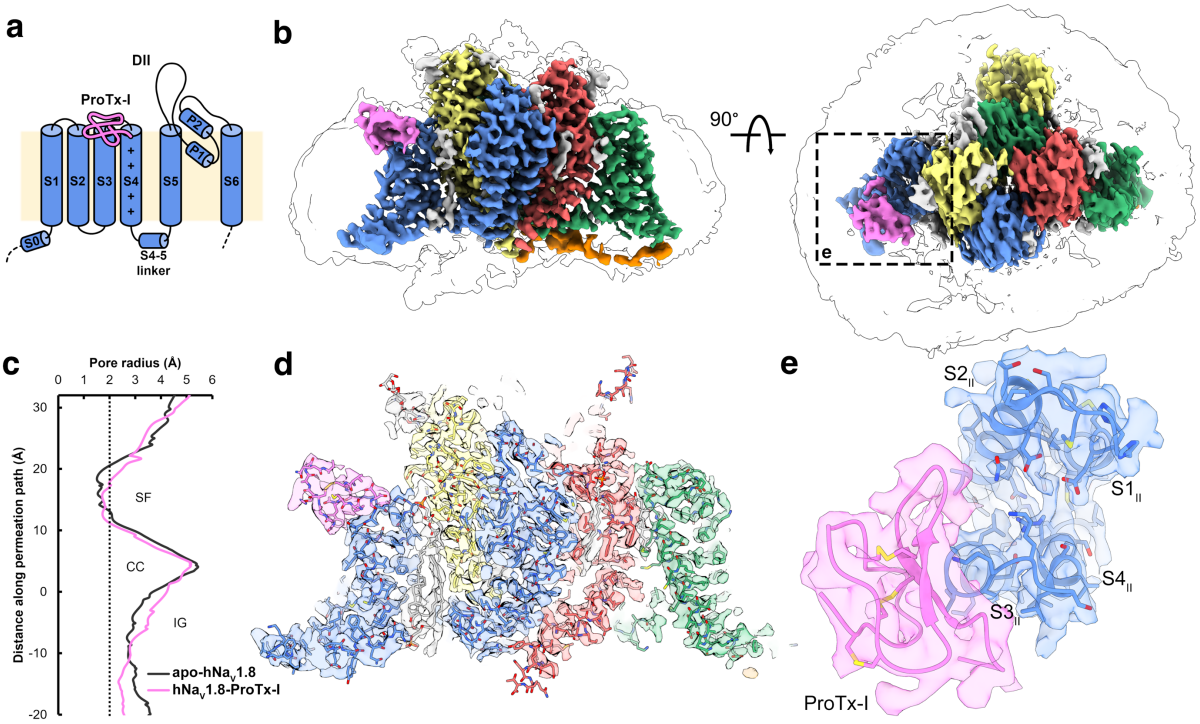

228
229
230 **Figure 3: Overall architecture and reconstruction of hNaV1.8-ProTx-I complex**
231 **a** Schematic showing the positioning of ProTx-I (pink) on hNaV1.8 VSD_{II}. **b** Side and extracellular views
232 of the final hNaV1.8-ProTx-I complex map, colored as in Figure **1c** with ProTx-I in pink; the dashed box
233 highlights the region binding ProTx-I. **c** Pore radius for the hNaV1.8-ProTx-I complex (pink) together
234 with apo-hNaV1.8 (black). **d** Model-to-map fit for a central cross-section of hNaV1.8-ProTx-I, and **e**
235 extracellular view of the fitted map in the ProTx-I-binding region.
236
237 Density for ProTx-I is clearly visible in the refined map; consistent with its electrophysiological
238 effects as a gating modifier and previous structure-activity relationship studies,[26] ProTx-I binds
239 to the S3-S4 linker on VSD_{II} (Figure 3b,d,e). The local resolution allowed the principal
240 backbone of the peptide to be traced, which, with the assistance of the discernible β-loop near
241 the peptide C-terminus, was sufficient to model ProTx-I into the map using an available NMR
242 model (see Methods). The resolution of the ProTx-I portion of the map is highest immediately
243 abutting the channel (likely due to stabilising interactions) and is attenuated in the more distant
244 regions (Supplementary Figure 6c); this reduction in density in the more peripheral regions is
245 a common feature of cryoEM studies of peptide-Na_V complexes.[30,33] Evidence from
246 mutagenesis experiments demonstrates that ProTx-I can also bind to hNaV1.7 VSD_{IV},[26]
247 although electrophysiological recordings have not demonstrated that ProTx-I has any effect
248 on channel inactivation thresholds that are typically governed by VSD_{IV}. Despite high local
249 resolution, we do not observe any density for ProTx-I above VSD_{IV} in the hNaV1.8-ProTx-I
250 structure, noting that the S1-S2 and S3-S4 linker regions on VSD_{IV} are poorly conserved
251 between hNaV1.7 and hNaV1.8 (Supplementary Figure 1).
252
253 ProTx-I is partly buried in the membrane. This interaction is mediated by a set of aromatic and
254 aliphatic residues (W5, L6, W27, W30) that together form a 'hydrophobic patch', which is
255 commonly observed in ICK peptides[43] (Figure 4a; Supplementary Movie 3) and explains prior
256 observations that ProTx-I shows some affinity for model membranes, especially anionic
257 membranes.[22] Tryptophan, in particular, is known to preferentially bind to the acyl carbonyl
258 groups at the lipid-water interface;[44] these residues are proposed to anchor the peptide to the

membrane and orientate it for interaction with the Na_V VSDs.[45] ProTx-I shows only small conformational changes with respect to its unbound structure, as would be expected for an ICK peptide where the disulfide bonding network maintains rigidity in the peptide core (Supplementary Figure 8a). The C-terminus is repositioned so as not to clash with the S3-S4 loop and permits the F34 sidechain access to the membrane.

The $hNa_V1.8$-ProTx-I structure shows several points of interaction between the peptide and $hNa_V1.8$ VSD_{II} (Figure 4). The membrane-embedded W27 sidechain partially inserts in the cleft formed by the S1/S2 and S3/S4 segments adjacent to I702 on S2 and G745 on S3, while the V29 sidechain is positioned directly on top of the S3 helix at V746/A747, likely hindering movement of this segment during activation (Figure 4b). The structure places the $S3_{II}$ V746 sidechain directly below ProTx-I, and its replacement by the bulkier leucine in $hNa_V1.1$-1.7 may hinder peptide binding and contribute to the slight increase in potency against $Na_V1.8$.

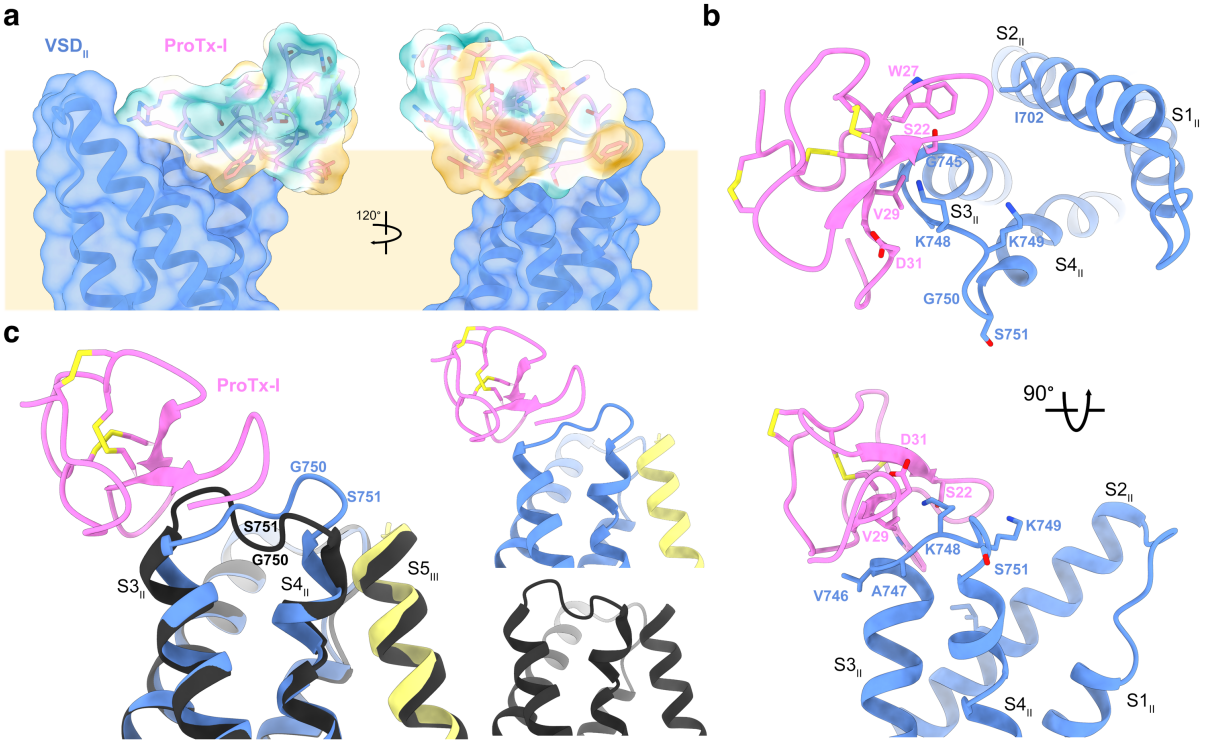

Figure 4: Interactions of ProTx-I with $hNa_V1.8$ and the membrane
a ProTx-I surface colored by hydrophobicity showing insertion of the hydrophobic patch into the membrane region (tan). Polar residues are indicated in teal, hydrophobic residues are indicated in gold. **b** Two views of the VSD_{II}-ProTx-I binding interface showing W27 sidechain partially inserting into the S2/S3 cleft, V29 sitting atop $S3_{II}$ at V746 and A747, and the K748 sidechain on the VSD_{II} S3-S4 linker in range to interact with the ProTx-I D31 and S22 sidechains. **c** (left) Overlay of the VSD_{II} S3-S4 linker position in the $hNa_V1.8$-ProTx-I complex (color scheme as in Figure 3a) and apo-$hNa_V1.8$ (black) showing inward movement towards the S4 helix, and (right) separated comparison of S3 and S4 helix positions

The VSD_{II} S3-S4 loop in the apo-$hNa_V1.8$ map is of relatively lower resolution, which made tracing the loop backbone challenging; by contrast, the local resolution in this region of the $hNa_V1.8$-ProTx-I complex map was improved (likely due to stabilisation from the interaction with ProTx-I) and allowed straightforward tracing of the S3-S4 loop backbone at a higher threshold level (Supplementary Figure 8b). Comparing the two structures shows that the binding of the toxin induces an inward movement of the top of the S3 helix together with a corresponding movement of the S3-S4 linker towards the pore domain (Figure 4c and Supplementary Movie 4). This redirection of the S3-S4 linker due to ProTx-I binding propagates along its length such that G750 and S751 now sit directly atop S4 and adjacent to

the pore domain, potentially hindering translocation of S4. This movement positions two adjacent lysine sidechains on the S3-S4 linker (K748 and K749, which are unique to hNa$_V$1.8; see Discussion) upwards; the first of these lysine sidechains is positioned close to polar residues on ProTx-I (D31 and S22) where it may form hydrogen-bonding interactions. These observations are consistent with structure-activity studies of ProTx-I. A tethered-toxin alanine scan of ProTx-I against Na$_V$1.7 identified multiple residues that significantly modified peptide activity (including L6, W27, V29, W30, and D31).[26] The structure shows that many of these residues either form direct contacts with the channel or form part of the hydrophobic face that anchors the peptide to the membrane (Figure 4a). Intriguingly, performing the same experiment with Na$_V$1.2 shows an expanded pharmacophore compared with Na$_V$1.7, with R3, W5, S22, R23, G32 also contributing to channel inhibition and suggesting that ProTx-I can adopt different binding modes depending on the Na$_V$ isoform that it is targeting.[24]

Mutagenesis experiments focusing on the channel have also explored the Na$_V$-ProTx-I interaction. An alanine scan of S3-S4 in a Na$_V$1.2-VSD$_{II}$/K$_V$1.2 chimera revealed several residues that modulated ProTx-I inhibition.[46] Mapping these residues to the hNa$_V$1.8-ProTx-I structure provides a partial justification of these results. Significant reductions in potency were observed on mutation of the hydrophobic residues at the top of S3$_{II}$; these correspond to V746 and A747 in Na$_V$1.8, and which are directly involved in ProTx-I binding (Figure 4b). Large changes were also observed for residues at the top of S4$_{II}$, equivalent to S751 and S753 in hNa$_V$1.8, which do not directly interact with ProTx-I in our structure but may instead relate to the inward push on the S3-S4 linker after binding.

Taken together, these structures justify prior structure-activity data as well as the observed pharmacological properties of ProTx-I on voltage-gated sodium channels. ProTx-I is observed to wrap around the top of the S3$_{II}$ helix, and inhibition is also likely mediated by the inward shift of the VSD$_{II}$ S3-S4 linker, which potentially restricts movement of the S4$_{II}$ helix. The positioning of residues which, in the hNa$_V$1.8-ProTx-I structure, do not form direct interactions, also provides hints as to the relative promiscuity of ProTx-I towards hNa$_V$ isoforms (discussed below).

Discussion

This study reports the cryoEM structures of apo-hNa$_V$1.8 and a hNa$_V$1.8-ProTx-I complex and provides insights into the mechanism of channel inhibition by ProTx-I, as well as a useful point of comparison with other structures. ProTx-I was observed to bind to VSD$_{II}$, with no density observed around VSD$_{IV}$, despite evidence from mutagenesis experiments.[26] The addition of ProTx-I seemed to stabilize hNa$_V$1.8 resulting in a better quality and higher resolution map, including in the peptide-binding region of the channel.

The decision to co-express with β-subunits was motivated by low expression yields of hNa$_V$1.8 and poor particle distribution on the grid; we were also keen to minimize the volume of cell culture required to obtain sufficient particles for cryoEM reconstruction, which can reach 40 L in some cases.[47] The β4-subunit was selected based on evidence that it interacts with hNa$_V$1.8 and affects activation and inactivation potentials.[35] However, no significant increase in the expression yield was seen and in subsequent purification and data collection steps only the hNa$_V$1.8 α-subunit was identified. A cryoEM structure of hNa$_V$1.1 together with β4 was able to resolve the β4 extracellular domain even as the co-expressed β3-subunit was not visible and demonstrated direct linking of β4 to the Na$_V$1.1 α-subunit via a disulfide bond to the VSD$_{II}$ S5-S6 extracellular loop.[39] hNa$_V$1.8 lacks the counterpart cysteine at this position required for disulfide bonding, which is likely to significantly weaken the interaction with β4; further investigation will be required to reveal the mechanism of gating modification of hNa$_V$1.8 by β4. Initial preparations produced homogeneous and good-quality particles, but in insufficient amounts to proceed with cryoEM. Since biochemical approaches did not significantly improve

the yield of hNa$_V$1.8, and we wished to avoid more drastic interventions (such as chimeras), we investigated different types of grids to optimise particle density and quality. The use of support films can drastically increase particle retention after blotting compared with conventional holey carbon grids[48] and we found that grids with monolayer graphene support showed the most initial promise. Further optimisation of the freezing conditions led to grids with a homogenous distribution of particles (Supplementary Figure 3c) obtained from as low as 1.5 L cell culture and ultimately resulted in all the high-resolution reconstructions presented in this paper.

The structures of apo-hNa$_V$1.8 revealed a large hinging movement of the VSD$_I$ S4-S5 linker that was resolvable in two separate classes (Figure 2). This VSD$_I$ S4-S5 linker movement is not observed between the previously determined apo-hNa$_V$1.8 and hNa$_V$1.8-A-803467 complex structures,[36] despite the flexibility shown in VSD$_I$ S1-S4. By contrast the VSD$_I$ S4-S5 linker is consistently found tucked in closely to VSD$_{II}$ S5 and S6, as it is in other Na$_V$ structures, while the S6$_I$ helix is also positioned more closely into the pore. Notably, however, similar position shifts are observed between wild-type hNa$_V$1.7 and hNa$_V$1.7-M11.[42] Previous work ascribed the comparative flexibility of VSD$_I$ to unique mutations in hNa$_V$1.8 VSD$_{II}$ S5 and identified two mutants (K806M and L809F) near the VSD$_{II}$ S5-VSD$_I$ interface that individually and collectively shift the voltage of activation to more polarised potentials.[36] Since we were unable to resolve VSD$_I$ in our structures we are unable to confirm the influence of these residues on VSD$_I$ flexibility, but we do observe an inward and upward shift of the VSD$_{II}$ S5 and S6 helices that justifies the connection between VSD$_I$ positioning and channel gating properties.

The unusual movements of the VSD$_I$ S4-S5 linker and S6 helix seen in our structures prompted closer examination of this region. Both regions are highly conserved across human Na$_V$1.1-1.8, although hNa$_V$1.9 shows lower sequence identity (Supplementary Figure 1). Aside from hNa$_V$1.9, only hNa$_V$1.8 has any mutations to the VSD$_I$ S4-S5 linker, with Val instead of Thr at position 234, and His replacing Glu at position 241. V234 points away from the rest of the channel and does not form any interactions except to solvent or detergent, but H241 is orientated towards the conserved E402 and Q403 residues on VSD$_I$ S6 (Supplementary Figure 9). When the VSD$_I$ S4-S5 linker is in the conventional tucked position, the His/Glu sidechain is close enough to interact with these polar residues.[36] Both Glu and His are capable of simultaneously donating and accepting hydrogen bonds, but the imidazole ring on the His sidechain imposes additional geometric restraints; the Glu-His mutation observed at this position in hNa$_V$1.8 may therefore affect the ability to form stabilizing interactions with VSD$_I$ S6 and may contribute to the lability of this region that was observed in our data.

The hNa$_V$1.8-ProTx-I structure is obtained at higher resolution than apo-hNa$_V$1.8, which allows an additional extracellular loop to be modelled into this map. The complex structure demonstrates binding of the peptide to the channel by wrapping around the top of the S3$_{II}$ helix. This interaction is mediated by anchoring of the peptide to the membrane via an external hydrophobic patch, together with acidic and polar residues that can potentially form hydrogen bonds with a lysine residue (unique to Na$_V$1.8) on the VSD$_{II}$ S3-S4 linker. The binding of ProTx-I induces an inward shift of the VSD$_{II}$ S3-S4 linker such that it partially repositions on top of the S4$_{II}$ helix, which we hypothesize hinders the movement of S4$_{II}$ during activation and justifies the gating-modifier properties of ProTx-I.

Comparing the hNa$_V$1.8-ProTx-I structure to other structures of gating-modifier peptides bound to Na$_V$s shows some similarities and differences in their modes of action. A cryoEM study of the gating-modifier peptide Huwentoxin-IV in complex with a nanodisc-bound NaChBac-Na$_V$1.7-VSD$_{II}$ chimera shows that the peptide is similarly orientated by its membrane-inserted hydrophobic patch to present polar residues towards the channel, particularly the K32 sidechain ‘stinger’ which is proposed to enter the VSD$_{II}$ cleft and come into proximity with negatively charged residues E822, D827, and E829.[49] This stinger

interaction mechanism is maintained when Huwentoxin-IV binds to the channel in the resting conformation.[32] Notably, in $hNa_V1.8$, D827 is modified to lysine while E829 is replaced by glycine; $hNa_V1.8$ additionally has a second lysine at K748, replacing valine in $hNa_V1.7$. The replacement of so many negatively charged residues in $hNa_V1.7$ by positive or neutral residues in $Na_V1.8$ would be sufficient to abolish these interactions and explain why $hNa_V1.8$ is resistant to Huwentoxin-IV.[50] It also justifies the lack of a similar 'stinger' strategy by ProTx-I in its inhibition of $hNa_V1.8$.

A similar chimeric strategy was used to obtain structures of *Thrixopelma pruriens* ICK peptide Protoxin-II in complex with $Na_V1.7$-VSD_{II}, which additionally revealed both activated and deactivated conformations.[31] While ProTx-I shows only mild selectivity towards $Na_V1.8$ compared with other isoforms, Protoxin-II is notable for its potency (IC_{50} = 0.3 nM) and selectivity (>100-fold) in favour of $hNa_V1.7$. As with the $hNa_V1.8$-ProTx-I structure, a prominent tryptophan sidechain partitions into the VSD_{II} S2-S3 cleft where it interacts with nearby hydrophobic residues (Figure 4b). Similar to Huwentoxin-IV, Protoxin-II inserts a lysine residue sidechain to interact with E811, but additionally projects its R22 sidechain towards the acidic residues on the S3-S4 linker. The involvement of the arginine sidechain is of interest because ProTx-I also has an arginine at an equivalent position (R23), and which was identified as an important residue in targeting $Na_V1.2$.[24] The map density for this loop is not sufficient for confident placement of the arginine sidechain (suggestive of regional flexibility), but the hydrogen-bonding partner residues E694 and Q698 on $S2_{II}$ are within range for these interactions to occur and present an additional possible binding mode for Na_V subtypes with acidic and polar residues in these positions. Notably, in $hNa_V1.7$ the equivalent positions (E694 and Q698) are replaced by Lys and Ala, respectively, which would abolish any potential interactions with ProTx-I R23.

Here, the cryoEM reconstructions of apo- and ProTx-I-bound $hNa_V1.8$ provide important insights into the versatile mechanisms that ProTx-I and other gating-modifier peptides have at their disposal to affect Na_V gating. This was enabled by the use of monolayer graphene support that allowed 3D reconstructions from relatively low concentrations of protein stemming from small volumes of cell culture, which may be beneficial for studies of other hNa_Vs and similarly challenging proteins. These results will assist in the development of novel analgesic drugs targeting $hNa_V1.8$, as well as aiding the structural characterization of peptide-Na_V complexes yet to be determined.

Methods

Isoform and cloning of $hNa_V1.8$ and β4

The $hNa_V1.8$ sequence (Supplementary Figure 1) used in this study was obtained from GenBank (NM_006514.3; the current canonical sequence NM_006514.4 has M1713 in place of Val, which does not significantly affect the electrophysiological properties of the channel).[36] The $hNa_V1.8$ sequence was N-terminally tagged with FLAG-tag, Twin-Strep-tag and a TEV protease site. The β4 sequence used in this study was obtained from GenBank (NM_174934.3) and C-terminally tagged with a TEV protease site and 6xHis-tag. The codon-optimised DNA was cloned into pcDNA3.1(+).

Transient expression of $hNa_V1.8$ and β4

HEK293 cells (FreeStyle 293-F, Gibco) were seeded at ~0.3 x 10^6 cells/mL into 3 L of FreeStyle 293 Expression Medium (Gibco) in a baffled polycarbonate 5 L Erlenmeyer flask and incubated at 37°C with 8% CO_2 at 110 rpm. After 3 days, fresh media prewarmed to 37°C was added to dilute the cells to 2 x 10^6 cells/mL. A total of 1.1 mg/L of DNA was used at a 2:1 ratio of $hNa_V1.8$ to β4 and was mixed into 90 mL of Opti-MEM Reduced Serum Medium (Gibco). A total of 10 mL (1 mg/mL in PBS) of PEI Max 40 kDa (Polysciences Inc.) was added

to the DNA and incubated for 20 min at room temperature. The cells were transiently co-transfected and harvested after 42 h at 800 × *g* for 30 min at 4°C. The ~35-40 g wet cell pellet was flash frozen in liquid nitrogen and stored at -80°C.

Protein purification of apo-hNa$_V$1.8

A 35 g HEK293 cell pellet, equivalent to 3 L of cells, was homogenized in 60 mL of buffer A (165 mM NaCl, 27.5 mM HEPES pH 7.5, 2 mM $MgCl_2$, 11% glycerol, 10 mM EDTA, and 3 x Pierce Protease Inhibitor Tablets (Thermo Scientific) supplemented with 5 units/mL of Benzonase (Millipore)) by plunging on ice in a glass Dounce tissue grinder with a large clearance pestle. The homogenate was diluted to 120 mL with buffer A and plunged on ice again with a small clearance pestle. The homogenate was diluted further with buffer A to a protein concentration of ~11 mg/mL (as determined by spectrophotometry using a Thermo Scientific NanoDrop). The membrane was solubilized for 2 h at 4°C on a roller shaker at 30 rpm in 1% n-dodecyl-B-D-maltoside (DDM) (GoldBio), 0.2% CHS (Anatrace) by adding 10X solubilization buffer (10% DDM, 2% CHS) for a final protein concentration of ~10 mg/mL. The bulk of the cellular debris was pelleted at 4,347 × *g* using an Eppendorf 5910R centrifuge for 10 min at 4°C. The supernatant was clarified further by ultracentrifugation with a Beckman Optima L ultracentrifuge equipped with a SW 32 Ti rotor at 25,000 rpm (r_{av} 76,800 × *g*) for 30 min at 4°C.

A 2 mL column volume (CV) of ANTI-FLAG M2 Affinity Gel (Millipore) was equilibrated in a gravity flow column with 2 CVs of buffer B (150 mM NaCl, 25 mM HEPES pH 7.5, 0.06% (w/v) glyco-diosgenin (GDN) (Anatrace)). The supernatant was mixed with the M2 affinity gel for 1 h at 4°C on a roller shaker at 5 rpm. After collecting the flow through by gravity, the affinity gel was washed gradually into buffer B in the following 5 CVs buffer A and buffer B ratios: 50:50, 25:75, 12.5:87.5, 5:95 and 0:100. Protein was eluted by mixing the M2 affinity gel with 5 CVs of buffer B supplemented with 200 µg/mL of FLAG peptide for 30 min at 4°C.

For size exclusion chromatography, two eluate fractions were loaded onto a Superose 6 Increase 10/300 GL column (Cytiva) connected to an ÄKTA pure system (Cytiva) in buffer C (150 mM NaCl, 25 mM HEPES pH 7.5, 0.006% (w/v) GDN) (Supplementary Figure 2a). Eluate 1 consisted of the first 2 mL eluted from the FLAG column; Eluate 2 consisted of the remaining FLAG eluate, concentrated to 0.5 mL in a 4 mL 100 kDa MWCO Amicon Ultra centrifugal filter (3,000 × *g* at 4°C). The flow rate was 0.7 mL/min at 4°C. Fractions 12-17 (11.8-14.8 mL) from both eluates were pooled and concentrated to 0.5 mL with a 4 mL 100 kDa MWCO Amicon Ultra centrifugal filter (3,000 × *g* at 4°C). The pooled fractions were again purified by size exclusion chromatography using the above method. Finally, fractions 13-15 (12.4-13.9 mL) were pooled and concentrated as before to 60 µL at ~0.4 mg/mL.

Addition of ProTx-I to apo-hNa$_V$1.8

Performed similarly to the forementioned protocol with the following changes. A 20 g HEK293 cell pellet, equivalent to 1.5 L of cell culture, was homogenized. Fractions 13-15 (12.4-13.9 mL) were pooled and concentrated to 250 µL at ~0.07 mg/mL. The concentrated apo-hNa$_V$1.8 was mixed with 25 µL of 0.5 mM (2 mg/mL) ProTx-I (Smartox Biotechnology) in 1 M HEPES pH 7.4 for a final concentration of 45 µM and incubated on ice for 30 min. The mixture was concentrated to 100 µL at ~0.15 mg/mL.

Negative staining

All samples were negatively stained following an established protocol.[51] Briefly; 3 µL of sample, ranging between 0.01-0.05 mg/mL, was pipetted onto glow-discharged carbon-coated 200-mesh Gilder Cu grids (Ted Pella). Excess sample was removed with filter paper, washed 5 times with 50 µL Milli-Q water drops, and finally stained with two 50 µL drops of 0.75% uranyl

formate (Electron Microscopy Sciences) and excess stain was vacuum aspirated. Grids were carbon-coated using a Leica ACE200, negatively glow charged using a PELCO easiGlow (Ted Pella) prior to addition of sample and stain was freshly prepared. All grids were imaged with a JEOL JEM-2100F TEM equipped with a Gatan OneView 4k x 4k camera. Negative stain 2D class averages (Supplementary Figure 2d) were calculated using Relion 3.1.[52]

CryoEM grid freezing

Quantifoil R2/4 300 mesh Au grids with monolayer graphene support film (Graphenea) were negatively glow discharged using a PELCO easiGlow (Ted Pella) with the monolayer graphene (front) facing up. A Leica EM GP2 set to 10°C and 96% humidity was used to freeze the grids. For apo-hNa$_V$1.8, 0.4 mg/mL sample was diluted with buffer C to 0.25 mg/mL and 3 µL was applied to the front of the grid and incubated for 60 s before front blotting for 3 s. For the hNa$_V$1.8-ProTx-I complex, 3 µL of 0.15 mg/mL sample was applied to the front of the grid and blotted as before. Grids were plunge frozen in liquid ethane and stored in liquid nitrogen.

CryoEM data collection

All movies were collected with a 300 kV FEI Titan Krios microscope equipped with a Gatan K3 direct electron detector. For apo-hNa$_V$1.8, super-resolution movies were collected using SerialEM[53] at a pixel size of 0.839 Å/pixel with a total dose of 60 e^-/ Å^2 spread over 60 total frames, with a defocus range of -1 to -2.5 µm and a 100 µm objective aperture. Energy filter slit width was set to 20 eV. The hNa$_V$1.8-ProTx-I acquisition was performed similarly with the following changes: data was collected at a pixel size of 0.827 Å/pixel with a defocus range of -1 to -2 µm. Full data collection parameters are highlighted in Supplementary Table 1.

CryoEM data processing of apo-hNa$_V$1.8

The processing pipeline is described in Supplementary Figure 4. Briefly; 13,124 movies were imported into CryoSPARC 4.2[54] for patch motion correction[55] and patch contrast transfer function (CTF) estimation. 13,006 micrographs were selected for blob picking using circular and elliptical templates resulting in 4,878,994 particle coordinates. Selected 2D classes were utilized for template picking resulting in 11,792,840 particle coordinates. After multiple rounds of 2D classifications, a subset of particles showing different views of apo-hNa$_V$1.8 were selected for *ab initio* initial 3D model building. Two 3D classes were selected and used as references to parse particles via heterogeneous refinement. Eventually 67,333 particles were used for non-uniform refinement[56] to create a 3.5 Å map. This map was used for template picking resulting in 12,107,700 particle coordinates.

Subsequent 2D classifications, 3D refinements, and 3D classifications resulted in a non-uniform refined and sharpened reconstruction at an overall resolution of 3.2 Å from 120,821 particles. 3D variability analysis[57]resulted in maps with varied conformations from distinct particles which were used for *ab initio* initial 3D model building. Two classes were subjected to non-uniform refinement and resulted in two distinct conformations of the VSD$_I$ S4-S5 linker as Class I with 84,466 particles and Class II with 82,542 particles at overall resolutions of 3.24 Å and 3.22 Å, respectively. The initial 3D model of Class II was used to refine a final sharpened map of apo-hNa$_V$1.8 with all 120,821 particles at an overall resolution of 3.12 Å.

CryoEM data processing of hNa$_V$1.8-ProTx-I

The processing pipeline is described in Supplementary Figure 6. Processing of the hNa$_V$1.8-ProTx-I dataset was performed similarly to the apo-hNa$_V$1.8 dataset with the following changes. 15,400 movies were processed using CryoSPARC 4.4. Template picking using the final apo-hNa$_V$1.8 map resulted in 10,509,847 particle coordinates for subsequent processing. After multiple rounds of 2D classifications, a subset of particles showing different views of

hNa$_V$1.8-ProTx-I were selected for *ab initio* initial 3D model building. A subset of 197,157 particles were used for non-uniform refinement into a 3D reconstruction at an overall resolution of 2.9 Å. Subsequent 2D classifications, 3D refinements, and 3D classifications resulted in a non-uniform refined and sharpened hNa$_V$1.8-ProTx-I reconstruction at an overall resolution of 2.76 Å from 267,708 particles. Focus refinement of VSD$_{I-II}$, as well as 3D classification did not aid in resolving VSD$_I$ or increasing the resolution of the ProTx-I binding region.

Model building, refinement and validation

hNa$_V$1.8 from PDB 7WFW[36] was rigid body fitted into the final apo-hNa$_V$1.8 map using ChimeraX. No density for β4 was observed and therefore was not modelled. The apo-hNa$_V$1.8 model was modified with M1713V, glycosylation sites were adjusted as necessary and the VSD$_I$ S4-S5 linker was positioned to best fit the map using *Coot*.[58] Additionally, 7WFW was found to contain a mutation (S894F) that differs from the canonical hNa$_V$1.8 sequence (NM_006514.3 and NM_006514.4), which was updated in our model. Cholesterol and bound lipids from PDB 7WE4 were used for model building. The model was refined in *Coot* and subsequently refined against the corresponding map using *Phenix* real-space refinement.[59] Models for Class I and II were initially built using an earlier apo-hNa$_V$1.8 model and similarly refined as described.

Modeling for hNa$_V$1.8-ProTx-I used an earlier apo-hNa$_V$1.8 model along with a single ProTx-I model from the NMR ensemble PDB 2M9L[24] and both were rigid body fit into the hNa$_V$1.8-ProTx-I map using ChimeraX.[60–62] Multiple orientations of ProTx-I were sampled to optimize the model-to-map fit. Steps for adjustments and refinements were performed similarly to apo-hNa$_V$1.8.

Model validations were performed using *Phenix* and MolProbity.[63,64] Statistics are available in Supplementary Table 1. Pore path and radius were determined using MOLEonline.[65] All figures were prepared with UCSF ChimeraX, Fiji,[66] Adobe Photoshop and Microsoft PowerPoint. Supplementary movies were prepared with UCSF ChimeraX.

Atomic coordinates and cryoEM maps associated with this study have been deposited to the Protein Data Bank (https://www.rcsb.org/) under the accession number IDs 9DBK [apo-hNa$_V$1.8], 9DBL [Class I], 9DBM [Class II], 9DBN [hNa$_V$1.8-ProTx-I] and EM Data Bank (https://www.ebi.ac.uk/emdb/) under the accession number IDs EMD-46718 [apo-hNa$_V$1.8], EMD-46719 [Class I], EMD-46720 [Class II], 46721 [hNa$_V$1.8-ProTx-I], respectively.

Acknowledgements

The authors thank all members of the Gonen lab for helpful and critical discussions. This research was supported by the Department of Defense HDTRA1-21-1-0004 and the National Institute of General Medical Sciences, grant R35-GM142797.

References

1. Han, C. *et al.* Human Nav1.8: Enhanced persistent and ramp currents contribute to distinct firing properties of human DRG neurons. *J Neurophysiol* **113**, 3172–3185 (2015).
2. Akopian, A. N., Sivilotti, L. & Wood, J. N. A tetrodotoxin-resistant voltage-gated sodium channel expressed by sensory neurons. *Nature* **379**, 257–262 (1996).
3. Dib-Hajj, S. D. *et al.* Two tetrodotoxin-resistant sodium channels in human dorsal root ganglion neurons. *FEBS Lett* **462**, 117–120 (1999).
4. Renganathan, M., Cummins, T. R. & Waxman, S. G. Contribution of Nav 1.8 sodium channels to action potential electrogenesis in DRG neurons. *J Neurophysiol* **86**, 629–640 (2001).

5. Blair, N. T. & Bean, B. P. Roles of tetrodotoxin (TTX)-sensitive Na+ current, TTX-resistant Na+ current, and Ca2+ current in the action potentials of nociceptive sensory neurons. *J Neurosci* **22**, 10277–10290 (2002).
6. Choi, J. S. & Waxman, S. G. Physiological interactions between NA v1.7 and NA v1.8 sodium channels: A computer simulation study. *J Neurophysiol* **106**, 3173–3184 (2011).
7. Tan, Z. Y. *et al.* Tetrodotoxin-resistant sodium channels in sensory neurons generate slow resurgent currents that are enhanced by inflammatory mediators. *J Neurosci* **34**, 7190–7197 (2014).
8. Zimmermann, K. *et al.* Sensory neuron sodium channel Nav1.8 is essential for pain at low temperatures. *Nature* **447**, 855–858 (2007).
9. Faber, C. G. *et al.* Gain-of-function Nav1.8 mutations in painful neuropathy. *Proc Natl Acad Sci U S A* **109**, 19444–19449 (2012).
10. Huang, J. *et al.* Small-fiber neuropathy Nav1.8 mutation shifts activation to hyperpolarized potentials and increases excitability of dorsal root ganglion neurons. *J Neurosci* **33**, 14087–14097 (2013).
11. Duan, G. *et al.* A SCN10A SNP biases human pain sensitivity. *Mol Pain* **12**, 1–16 (2016).
12. Gonzalez-Lopez, E. *et al.* Homozygosity for the SCN10A polymorphism rs6795970 is associated with hypoalgesic inflammatory bowel disease phenotype. *Front Med* **5**, 1–8 (2018).
13. Bennett, D. L., Clark, X. A. J., Huang, J., Waxman, S. G. & Dib-Hajj, S. D. The role of voltage-gated sodium channels in pain signaling. *Physiol Rev* **99**, 1079–1151 (2019).
14. Rowe, A. H. & Rowe, M. P. Physiological resistance of grasshopper mice (Onychomys spp.) to Arizona bark scorpion (Centruroides exilicauda) venom. *Toxicon* **52**, 597–605 (2008).
15. Rowe, A. H., Xiao, Y., Rowe, M. P., Cummins, T. R. & Zakon, H. H. Voltage-Gated Sodium Channel in Grasshopper Mice Defends Against Bark Scorpion Toxin. *October* **441**, 441–447 (2013).
16. Ye, P. *et al.* Scorpion toxin BmK I directly activates Nav1.8 in primary sensory neurons to induce neuronal hyperexcitability in rats. *Protein Cell* **6**, 443–452 (2015).
17. McIntosh, J. M. *et al.* A new family of conotoxins that blocks voltage-gated sodium channels. *J Biol Chem* **270**, 16796–16802 (1995).
18. Ekberg, J. *et al.* μO-conotoxin MrVIB selectively blocks NaV1.8 sensory neuron specific sodium channels and chronic pain behavior without motor deficits. *Proc Natl Acad Sci U S A* **103**, 17030–17035 (2006).
19. Yang, M. & Zhou, M. μ-conotoxin TsIIIA, a peptide inhibitor of human voltage-gated sodium channel hNav1.8. *Toxicon* **186**, 29–34 (2020).
20. Priest, B. T., Blumenthal, K. M., Smith, J. J., Warren, V. A. & Smith, M. M. ProTx-I and ProTx-II: Gating modifiers of voltage-gated sodium channels. *Toxicon* **49**, 194–201 (2007).
21. Middleton, R. E. *et al.* Two Tarantula Peptides Inhibit Activation of Multiple Sodium Channels. *Biochemistry* **41**, 14734–14747 (2002).
22. Agwa, A. J. *et al.* Gating modifier toxins isolated from spider venom: Modulation of voltage-gated sodium channels and the role of lipid membranes. *J Biol Chem* **293**, 9041–9052 (2018).
23. Ohkubo, T., Yamazaki, J. & Kitamura, K. Tarantula toxin ProTx-I differentiates between human T-type voltage-gated Ca2+ channels Cav3.1 and Cav3.2. *J Pharmacol Sci* **112**, 452–458 (2010).
24. Gui, J. *et al.* A tarantula-venom peptide antagonizes the TRPA1 nociceptor Ion channel by binding to the S1-S4 gating domain. *Curr Biol* **24**, 473–483 (2014).
25. Laverne, V., Alewood, P. F., Mobli, M. & King, G. F. The Structural Universe of Disulfide-Rich Venom Peptides. in *Venoms to Drugs: Venom as a Source for the Development of Human Therapeutics* (ed. King, G. F.) 37–70 (Royal Society of Chemistry, 2015).
26. Rupasinghe, D. B. *et al.* Mutational analysis of ProTx-I and the novel venom peptide Pe1b provide insight into residues responsible for selective inhibition of the analgesic

drug target NaV1.7. *Biochem Pharmacol* **181**, 114080 (2020).
27. Pan, X. *et al.* Molecular basis for pore blockade of human Na+ channel Nav1.2 by the μ-conotoxin KIIIA. *Science (80-)* **363**, 1309–1313 (2019).
28. Jiang, D. *et al.* Structural basis for voltage-sensor trapping of the cardiac sodium channel by a deathstalker scorpion toxin. *Nat Commun* **12**, (2021).
29. Shen, H. *et al.* Structural basis for the modulation of voltage-gated sodium channels by animal toxins. *Science (80-)* **362**, 1–8 (2018).
30. Shen, H., Liu, D., Wu, K., Lei, J. & Yan, N. Structures of human Nav1.7 channel in complex with auxiliary subunits and animal toxins. *Science (80-)* **363**, 1303–1308 (2019).
31. Xu, H. *et al.* Structural Basis of Nav1.7 Inhibition by a Gating-Modifier Spider Toxin. *Cell* **176**, 702–715 (2019).
32. Wisedchaisri, G. *et al.* Structural Basis for High-Affinity Trapping of the NaV1.7 Channel in Its Resting State by Tarantula Toxin. *Mol Cell* **81**, 38-48.e4 (2021).
33. Clairfeuille, T. *et al.* Structural basis of a-scorpion toxin action on Nav channels. *Science (80-)* **363**, (2019).
34. Huang, G. *et al.* High-resolution structures of human Nav1.7 reveal gating modulation through α-π helical transition of S6IV. *Cell Rep* **39**, (2022).
35. Zhao, J., O'Leary, M. E. & Chahine, M. Regulation of Nav1.6 and Nav1.8 peripheral nerve Na+ channels by auxiliary β-subunits. *J Neurophysiol* **106**, 608–619 (2011).
36. Huang, X. *et al.* Structural basis for high-voltage activation and subtype-specific inhibition of human Nav1.8. *Proc Natl Acad Sci* 1–9 (2022) doi:10.1073/pnas.2208211119/-/DCSupplemental.Published.
37. Li, Z. *et al.* Structural Basis for Pore Blockade of the Human Cardiac Sodium Channel Nav1.5 by the Antiarrhythmic Drug Quinidine**. *Angew Chemie - Int Ed* **60**, 11474–11480 (2021).
38. Li, Z. *et al.* Structure of human Nav1.5 reveals the fast inactivation-related segments as a mutational hotspot for the long QT syndrome. *Proc Natl Acad Sci U S A* **118**, 1–7 (2021).
39. Pan, X. *et al.* Comparative structural analysis of human Nav1.1 and Nav1.5 reveals mutational hotspots for sodium channelopathies. *Proc Natl Acad Sci U S A* **118**, 1–7 (2021).
40. Pan, X. *et al.* Structure of the human voltage-gated sodium channel Nav1.4 in complex with β1. *Science (80-)* **362**, (2018).
41. Jiang, D. *et al.* Structure of the Cardiac Sodium Channel. *Cell* **180**, 122-134.e10 (2020).
42. Huang, G. *et al.* Unwinding and spiral sliding of S4 and domain rotation of VSD during the electromechanical coupling in Nav1.7. *Proc Natl Acad Sci U S A* **119**, 1–9 (2022).
43. Ferrat, G. & Darbon, H. An overview of the three dimensional structure of short spider toxins. *Toxin Rev* **24**, 359–381 (2005).
44. Khemaissa, S., Sagan, S. & Walrant, A. Tryptophan, an amino-acid endowed with unique properties and its many roles in membrane proteins. *Crystals* **11**, (2021).
45. Henriques, S. T. *et al.* Interaction of tarantula venom peptide ProTx-II with lipid membranes is a prerequisite for its inhibition of human voltage-gated sodium channel NaV 1.7. *J Biol Chem* **291**, 17049–17065 (2016).
46. Bosmans, F., Martin-Eauclaire, M.-F. & Swartz, K. J. Deconstructing voltage sensor function and pharmacology in sodium channels. *Nature* **456**, 202–208 (2008).
47. Fan, X., Huang, J., Jin, X. & Yan, N. Cryo-EM structure of human voltage-gated sodium channel Nav1.6. *Proc Natl Acad Sci* **120**, e2220578120 (2023).
48. Han, Y. *et al.* High-yield monolayer graphene grids for near-atomic resolution cryoelectron microscopy. *Proc Natl Acad Sci U S A* **117**, 1009–1014 (2020).
49. Gao, S. *et al.* Employing NaChBac for cryo-EM analysis of toxin action on voltage-gated Na+ channels in nanodisc. *Proc Natl Acad Sci U S A* **117**, 14187–14193 (2020).
50. Xiao, Y. *et al.* Tarantula huwentoxin-IV inhibits neuronal sodium channels by binding to receptor site 4 and trapping the domain II voltage sensor in the closed configuration. *J Biol Chem* **283**, 27300–27313 (2008).

51. Gonen, S. Progress Towards CryoEM: Negative-Stain Procedures for Biological Samples. in *cryoEM: Methods and Protocols* (eds. Gonen, T. & Nannenga, B. L.) 145–160 (Humana Press, 2021).
52. Scheres, S. H. W. RELION: Implementation of a Bayesian approach to cryo-EM structure determination. *J Struct Biol* **180**, 519–530 (2012).
53. Mastronarde, D. N. SerialEM: A program for automated tilt series acquisition on Tecnai microscopes using prediction of specimen position. *Microsc Microanal* **9**, 1182–1183 (2003).
54. Punjani, A., Rubinstein, J. L., Fleet, D. J. & Brubaker, M. A. CryoSPARC: Algorithms for rapid unsupervised cryo-EM structure determination. *Nat Methods* **14**, 290–296 (2017).
55. Rubinstein, J. L. & Brubaker, M. A. Alignment of cryo-EM movies of individual particles by optimization of image translations. *J Struct Biol* **192**, 188–195 (2015).
56. Punjani, A., Zhang, H. & Fleet, D. J. Non-uniform refinement: adaptive regularization improves single-particle cryo-EM reconstruction. *Nat Methods* **17**, 1214–1221 (2020).
57. Punjani, A. & Fleet, D. J. 3D variability analysis: Resolving continuous flexibility and discrete heterogeneity from single particle cryo-EM. *J Struct Biol* **213**, 107702 (2021).
58. Emsley, P., Lohkamp, B., Scott, W. G. & Cowtan, K. Features and development of Coot. *Acta Crystallogr Sect D Biol Crystallogr* **66**, 486–501 (2010).
59. Liebschner, D. *et al.* Macromolecular structure determination using X-rays, neutrons and electrons: Recent developments in Phenix. *Acta Crystallogr Sect D Struct Biol* **75**, 861–877 (2019).
60. Pettersen, E. F. *et al.* UCSF ChimeraX: Structure visualization for researchers, educators, and developers. *Protein Sci* **30**, 70–82 (2021).
61. Goddard, T. D. *et al.* UCSF ChimeraX: Meeting modern challenges in visualization and analysis. *Protein Sci* **27**, 14–25 (2018).
62. Meng, E. C. *et al.* UCSF ChimeraX: Tools for structure building and analysis. *Protein Sci* **32**, 1–13 (2023).
63. Davis, I. W. *et al.* MolProbity: All-atom contacts and structure validation for proteins and nucleic acids. *Nucleic Acids Res* **35**, 375–383 (2007).
64. Williams, C. J. *et al.* MolProbity: More and better reference data for improved all-atom structure validation. *Protein Sci* **27**, 293–315 (2018).
65. Pravda, L. *et al.* MOLEonline: A web-based tool for analyzing channels, tunnels and pores (2018 update). *Nucleic Acids Res* **46**, W368–W373 (2018).
66. Schindelin, J. *et al.* Fiji: An open-source platform for biological-image analysis. *Nat Methods* **9**, 676–682 (2012).